Corrosion Science 192 (2021) 109788

Contents lists available at ScienceDirect

Corrosion Science

journal homepage: www.elsevier.com/locate/corsci

Corrosion mechanism of Ti_2AlC MAX phase coatings under the synergistic effects of water vapor and solid NaCl at 600 °C

Zhenyu Wang [a,b,*], Guanshui Ma [b], Zhongchang Li [b], Haitao Ruan [a,b], Jianghuai Yuan [a,b], Li Wang [a,b], Peiling Ke [b], Aiying Wang [a,b,*]

[a] Ningbo Institute of Industrial Technology, Ningbo 315201, China
[b] Key Laboratory of Marine Materials and Related Technologies, Zhejiang Key Laboratory of Marine Materials and Protective Technologies, Ningbo Institute of Materials Technology and Engineering, Chinese Academy of Sciences, Ningbo 315201, China

ARTICLE INFO

Keywords:
A. Sputtered films
A. Ceramic
B. STEM
C. Interface
C. High temperature corrosion

ABSTRACT

The corrosion behavior of Ti_2AlC MAX phase coatings coated on 1Cr11Ni2W2MoV substrates in NaCl deposit in water vapor at 600 °C has been fully investigated. The results demonstrated that the substrates underwent serious corrosion, but the coatings performed better. The mass gain per unit area of coatings was less than 1/6 of substrates, because of the formed compact and uniform corrosion scale. Such dense corrosion scale was composed of $Na_xTi_yO_z$ fine grains with the size of 11 ± 0.4 nm and amorphous Al_2O_3 phases which self-healed the generated defects during corrosion, benefiting from the novel layered structure of MAX phase.

1. Introduction

Compared to the mild inland areas, the marine environment is a highly saline and humid atmosphere in which it contains lots of water vapor and NaCl particles. For most gas turbine or aircraft engines operating at 300–600 °C in marine environment, severe corrosion of compressor blades is already being one of the key factors that restrict their working performance, life and safety due to a synergistic effect of the water vapor and solid NaCl deposit [1,2]. Extensive works [3–6] have demonstrated that, for compressor blades, typical metals and their alloys like pure Fe, Fe-Cr alloy, pure Ti, Ti alloy suffered from the intermediate-/high temperature corrosion, which was strongly accelerated by small additions of NaCl salts. It was reported that the rapid corrosion was mainly attributed to the chemical reactions of the chloride salts deposit with the protective oxides. This led to the formation of porous non-protective scale with numerous voids and holes. Meanwhile, the generated HCl and Cl_2 gases during the chemical reaction could act as active catalyst of the corrosion progress to further erode the substrates [6,7].

In order to slow down the corrosion behavior induced by solid NaCl deposit in water vapor, single layered and multilayer protective coatings prepared by physical vapor deposition (PVD) technique have been attempted for the metallic compressor blades. Among the single layered coatings, TiN and TiAlN coatings were considered as preferred choice because of their good chemical inertness and thermal stability [8,9]. However, since these single layer nitride coatings were prepared by magnetron sputtering or cathodic vacuum arc technology, the presence of columnar structure and inherent defects (pinholes, voids, micro-cracks and macro-particles, etc.) could not be avoided. These defects would lead to the easier penetration of corrosion media (e.g., water vapor, oxygen or NaCl) and finally caused the local corrosion of substrate [10,11]. Moreover, under the synergistic effects of H_2O/O_2 and NaCl, the initial formed dense oxide scale (titanium oxide) for the Ti-based coatings was rapidly consumed to generate porous sodium titanate ($Na_xTi_yO_z$) scale containing a large amount of defects [9].

Considering the continuous columnar microstructure could be interrupted via the introduce of metal sublayers, metal/nitride multilayer coatings benefit the superior protection than those of single layered coatings in marine environment. Nevertheless, high density of heterogeneous interface caused severe property degradation for multilayer coatings under the synthetic corrosive media of water vapor and solid NaCl at elevated temperature. Zhang et al. [12] investigated the corrosion process of TiAlN/Ti multilayer coating under NaCl-O_2-H_2O at 600 °C. The results indicated that the corrosion media quickly penetrated into the coating causing fast oxidation of the Ti sub-layer at raised temperatures accompanied with volume expansion. This eventually resulted in cracking and bending of the sublayers of TiAlN/Ti multilayer coatings, which accelerated both local corrosion of the substrates and

* Corresponding authors at: Ningbo Institute of Industrial Technology, Ningbo 315201, China.
E-mail addresses: wangzy@nimte.ac.cn (Z. Wang), aywang@nimte.ac.cn (A. Wang).

https://doi.org/10.1016/j.corsci.2021.109788
Received 13 July 2021; Received in revised form 20 August 2021; Accepted 21 August 2021
Available online 24 August 2021

coatings. Furthermore, they studied the corrosion behavior of the thicker Ti/TiN multilayer coating in NaCl-O_2-H_2O at 450 °C [13], where internal oxide also taken place within the TiN single layer. This was essentially harmful for the long-term protection of coatings. As a result, developing the high-performance protective coatings against the synergistic corrosion of water vapor and solid NaCl at intermediate/high temperature is still desirable to solve.

Ti_2AlC belongs to one of the ternary nanolaminated compounds of $M_{n+1}AX_n$ (MAX, n = 1–3) phases with the hexagonal structure (space group $P6_3/mmc$), where M represents an early transition metal, A is an element predominantly from Groups IIIA or IV, and X is C or N [14]. As known so far, the most significant characteristics of Ti_2AlC are excellent chemical and physical performances which have brought this material as the most practical MAX phase. The recognized low density of 4.11 g/cm^3 favors Ti_2AlC as the lightest Ti-based MAX phase materials among 211 series. In addition, Ti_2AlC shows the strongest candidates of MAX phases for intermediate/high-temperature applications in the form of bulk and coatings [15]. Other attracting features of the Ti_2AlC are well known as brittle-plastic transition at 1050 °C, high strength at elevated temperatures, excellent thermal shock and oxidation resistance, as well as good corrosion resistance [16,17]. Very recently, Ti_2AlC has been demonstrated to behave superior crack self-healing capabilities. For example, Yang et al. [18] claimed that superficial cracks and grooves of Ti_2AlC exhibiting the width of ≤ 10 μm were self-healed after 20 h oxidation at 1200 °C via dense Al_2O_3. Our results [19] indicated that the self-healing temperature of Ti_2AlC coatings could be further reduced to below 700 °C by A-site Sn solid solution. This makes Ti_2AlC suitable for protective coatings with high-performance for combined oxidation-/corrosion-resistant applications.

In our previous work [20], dense and predominantly single-phase Ti_2AlC coatings were successfully prepared by a combined arc/sputtering deposition technique. Until now, to our best knowledge, the corrosion behavior of MAX phase coatings in solid NaCl salt deposits in water vapor at 300–600 °C has not been fully examined and the corrosion mechanism has remained largely unexplored. In this work, we focused on the synergistic corrosion properties of Ti_2AlC coatings in solid NaCl deposits in water vapor at 600 °C for 75 h. Meanwhile, the corrosion behaviors of 1Cr11Ni2W2MoV substrates under both water vapor and NaCl deposits in water vapor and Ti_2AlC coatings under water vapor were also conducted, respectively, for comparison. Based on the observation of corrosion scale and the microstructural analyses of the coatings, the corrosion mechanism of Ti_2AlC coatings was discussed during corrosion process.

2. Experimental procedure

2.1. Ti_2AlC coatings preparation

The Ti_2AlC MAX phase coatings were deposited on martensitic stainless steel (MSS for short) substrates (1Cr11Ni2W2MoV; 10 mm × 10 mm × 2 mm) by combined arc/magnetron sputtering, followed by vacuum annealed-treatment. The nominal composition of MSS (%wt) was: C, 0.10–0.16; Mn, ≤ 0.60; Si, ≤ 0.60; Cr, 10.5–12.0; Ni, 1.40–1.80; W, 1.50–2.00; V, 0.18–0.30; Mo, 0.35–0.50; S, ≤ 0.020; P, ≤ 0.030, and the balance Fe. Substrates were ultrasonically cleaned with alcohol and acetone for 15 min, respectively, and then hung into the sample holder by Fe wires for coating preparation. Aluminum target (purity, 99.9%) and titanium target (purity, 99.9%) were used as magnetron sputtering source and cathodic vacuum arc source, respectively. Details of deposition progress and the schematic of system could be referred elsewhere [21]. To improve the adhesion strength and prevent the elements interdiffusion during annealing and corrosion progresses, all substrates were ion etched with Ar^+ for 60 min, and then a TiC interlayer with the thickness of ~ 1.6 μm was prepared by arc ion plating. During Ti-Al-C coating deposition, CH_4 and Ar with flowing rate ratio of Ar/CH_4 = 40/3 were applied as working gas. The substrates were planetary rotated in face of Al targets, 5 cm apart, to ensure all faces were uniformly coated. During deposition, Al and Ti targets with the power of 3.1 kW and 18 W, respectively, were applied. Deposition temperature was kept at 200 °C with a chamber pressure of 2.0 Pa. Substrate bias voltage of −150 V was performed during etching and deposition processes. After deposition, the deposited Ti-Al-C coatings were annealed to form Ti_2AlC MAX phase coatings at 700 °C for 1.5 h in a controlled vacuum of 1.0×10^{-3} Pa.

2.2. Corrosion test

Corrosion tests were conducted in a designed setup in flowing water vapor atmosphere at 600 °C. The device primarily contained a water vapor generation system and a heating system, as illustrated in Ref. [22]. Prior to test, saturated NaCl solution was sprayed on the two main surfaces of the as-deposited Ti_2AlC coatings with a spray bottle followed by drying with the box furnace. Then, repeating the above steps to control the deposited solid NaCl at a mass of 1 ± 0.1 mg/cm^2. When the tube furnace was heated to predetermined temperatures, flowing water vapor made by water vapor generator with a fixed rate of 1 ml/min was introduced into the setup. In order to obtain a pure water vapor reaction atmosphere, after the water vapor flowing for 1 h, the samples covered with NaCl salts were moved into the middle of furnace chamber. With various intervals, the corroded samples were taken out from the furnace, cooled down in air to room temperature, and weighted the mass gain by an analytical balance (0.01 mg precision, METTLER TOLEDO MS105/A). The whole corrosion test lasted for 75 h. Each test was repeated more than 6 times to ensure its accuracy.

2.3. Characterization methods

The microstructures of the as-deposited Ti_2AlC coatings and the samples after corrosion were examined using scanning electron microscope (SEM, FEI Quanta FEG 250) equipped with an Oxford energy-dispersive spectrometer (EDS), operated at 15 kV. X-ray diffraction (XRD) θ-2θ scans were obtained by a D8-Advance Brucker diffractometer with a Cu Kα radiation (λ = 1.5406 Å) to determine the phase structure. X-ray photoelectron spectroscopy (XPS) with Al Kα radiation ($h\nu$ = 1486.6 eV; Kratos Axis ULTRA DLD) was used to observe the compositions of corrosion scale on the samples. Prior to peak fitting, contaminated carbon with C 1s peak of 284.8 eV was applied to calibrate the binding energies. Cross-sectional transmission electron microscopy (TEM), selected-area electron diffraction (SAED) and high resolution TEM (HRTEM) were accomplished with a Talos F200X electron microscope operating at 200 kV. Furthermore, Z-contrast images and EDS elemental mappings were acquired in the scanning TEM high-angle-annular-dark-filed (STEM-HAADF) mode equipped with an EDS detector. The grain size of the as-deposited and the oxidized coatings was also analyzed using both TEM dark-field (DF) and scanning TEM low-angle-annular-dark-filed (STEM-ADF) imaging. TEM specimens were prepared by focused ion beam (FIB; Carl Zeiss, Auriga).

3. Results

3.1. Microstructural characterization

Fig. 1 illustrates the microstructure characterization of the as-prepared Ti_2AlC coatings. XRD θ-2θ scans (Fig. 1a) indicated that Ti_2AlC MAX phase was the dominant crystalline phases in addition to a small amount of purity phases including Ti_3AlC, TiC and $TiAl_x$. Thus, it could be concluded that nearly single-phase Ti_2AlC coatings were successfully obtained by the combined arc/sputtering technique here. Fig. 1b and c represents the surface and cross-sectional morphologies of Ti_2AlC coatings. The cross-sectional backscatter electron (BSE) image, together with the EDS line scanning results (Fig. 1b) revealed that the as-deposited coatings were homogenous, dense, and strongly bonded with

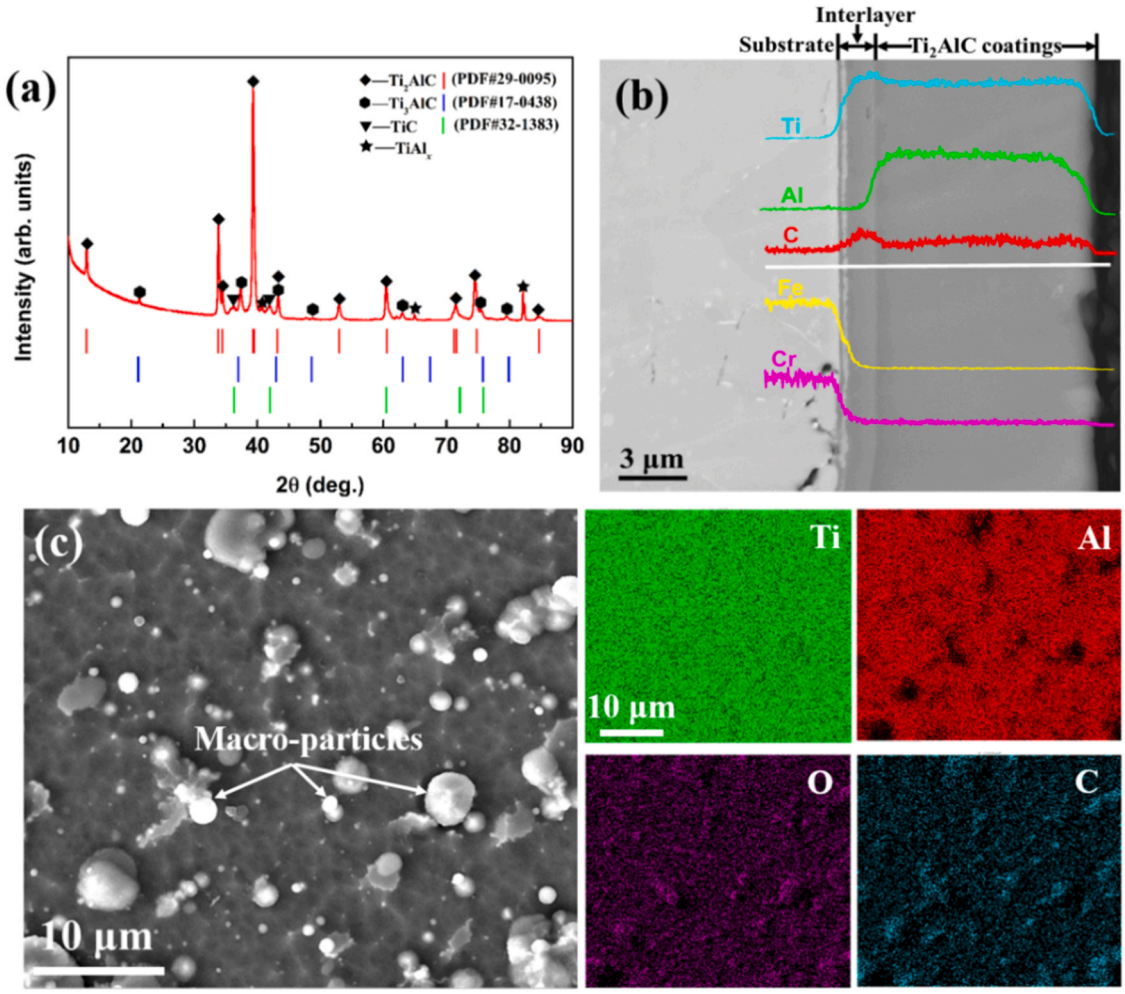

Fig. 1. (a) XRD patterns of the as-prepared coatings. (b) Cross-sectional morphologies (BSE mode) and corresponding line-scanning results of Ti (blue), Al (green), C (red), Fe (yellow), and Cr (magenta) signals along the marked white line. (c) Surface morphologies of the as-prepared Ti_2AlC coatings and corresponding Ti (green), Al (red), C (blue), O (magenta) elemental maps.

the substrate. In addition, the coatings behaved two layered structures: a ~ 1.6 μm thick inner TiC_x layer, and a ~ 10 μm thick outer Ti_2AlC layer. Benefiting from the presence of TiC layer, the bond interface between substrate and coating was relatively sharp and clear, without any defects, such as cracks and delamination, which contributed to the corrosion resistance of the coatings under harsh environments. With the surface morphology inspection (Fig. 1c), it could be seen that, in spite of existence of some macro-particles, the coatings exhibited much denser structure compared to the previous results where only single kind of deposition technique was used [23,24]. In view of the EDS mapping results, these macro-particles were evaluated to be enriched in Ti and poor in Al. This revealed that they are formed mainly by the ejection of Ti droplets during arc discharge of the Ti target, which was typical feature of the arc technique. Meanwhile, the macro-particles were also observed to be enriched in O and C, which might be ascribed to the strong reaction reactivity and adsorption effects with O and C for Ti elements.

Further TEM test is conducted to gain insight into the microstructure of the as-prepared Ti_2AlC coatings. As shown in Fig. 2a, the cross-section TEM image indicated that the coatings exhibited equiaxed grains with the dense structure. This could favor high thermal-stability and superior oxidation/corrosion resistance due to the significant reduced fast diffusion channels. Similar result was also reported in Ref. [21] where high-performance Cr_2AlC coatings were obtained against oxidation. The average grain size was calculated from the DF-TEM image (Fig. 2b) to be approximately 103 nm (Fig. 2c) by the nano-measurer software. The lattice structure of Ti_2AlC which belongs to a hexagonal close-packed structure (space group $P6_3/mmc$) is given in Fig. 2f, and the Ti, Al and C atoms occupy at 4f, 2d, and 2a Wyckoff positions, respectively. The atom stacking sequence of Ti_2AlC along [000*l*] direction can be characterized as ABABAB, in which the underlined letters refer to the Al atomic layers, and other letters correspond to the Ti atomic layers. The stacking sequence could be clearly observed in the atomic-resolution STEM image (Fig. 2e) of one Ti_2AlC grain (marked in Fig. 2d as "A") when the direction of electron beam was parallel to the [11$\bar{2}$0] zones. This are in accord with the structural configurations in the atomic model shown in Fig. 2f. However, the C atoms were not be resolved in STEM due to their weak diffraction power. The *c* lattice parameter calculated from the atomic-resolution STEM image (Fig. 2e) was 1.36 nm, in line with the standard value of the Ti_2AlC crystal.

3.2. Corrosion kinetics

Fig. 3 gives the mass gain dependences of corrosion time for 1Cr11Ni2W2MoV substrates and Ti_2AlC coatings exposed with two corrosive environments. The mass gain exhibited negative value in the initial 5 h of corrosion because of the volatilization of gaseous corrosion products and adsorbed water vapor. After 75 h corrosion under solid NaCl deposits in water vapor environment at 600 °C, the mass gains per unit area of the 1Cr11Ni2W2MoV substrates and Ti_2AlC coatings were

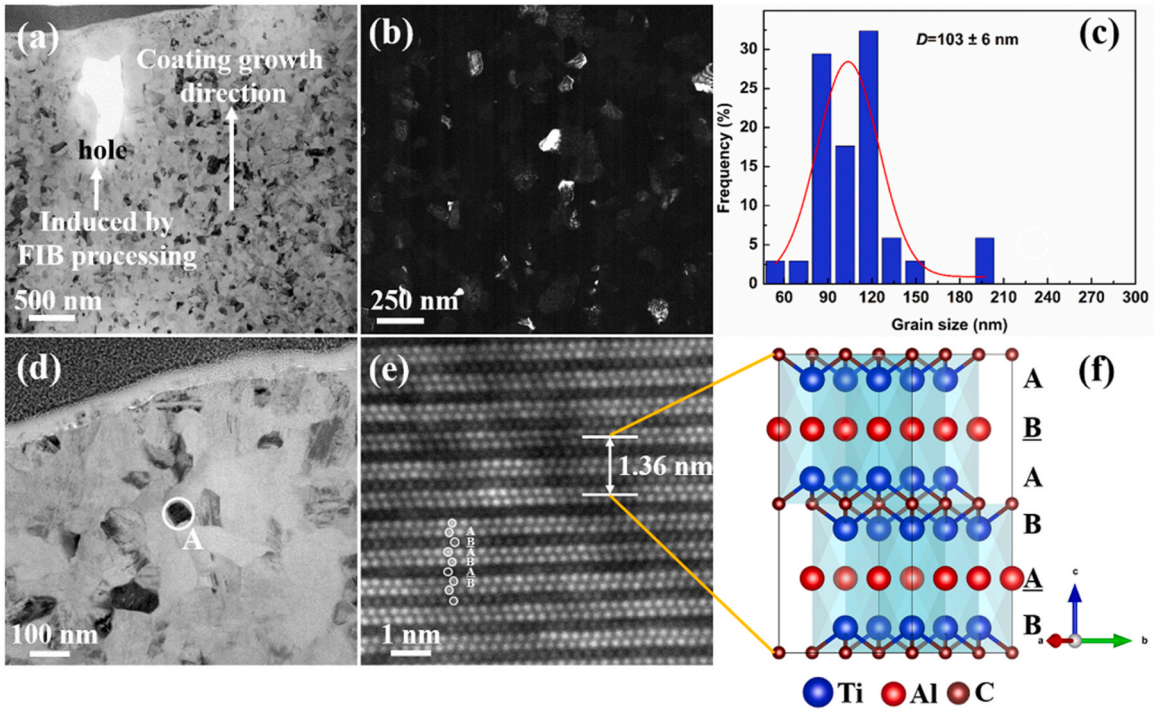

Fig. 2. (a) Cross-sectional TEM bright-field image and (b) TEM dark-field image of the as-prepared Ti_2AlC coatings. (c) The size distributions of the Ti_2AlC grains calculated by the results in (b). (d) Cross-sectional TEM bright-field image with higher magnification compared to (a). (e) The atomic arrangement STEM image of Ti_2AlC grain marked as "A" in (d), and (f) Unit cell of Ti_2AlC showing the octahedral of Ti_6C separated by Al layers with the C occupying the octahedral Ti coordination along $[11\bar{2}0]$ zone axis.

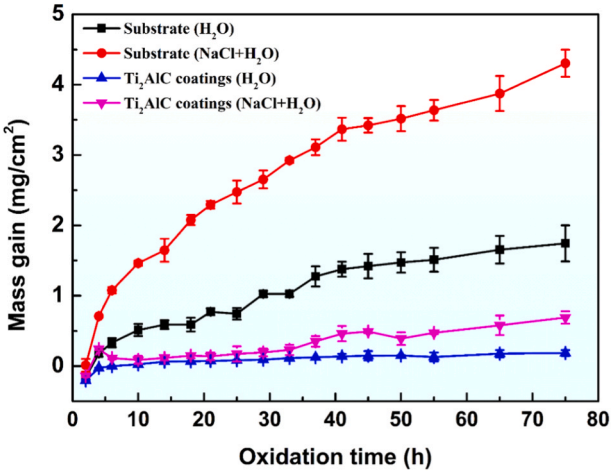

Fig. 3. Mass gain versus exposure time for 1Cr11Ni2W2MoV substrates and Ti_2AlC coatings exposed to H_2O and solid NaCl deposit in water vapor at 600 °C.

4.3 ± 0.19 mg/cm^2 and 0.69 ± 0.09 mg/cm^2, respectively, which were more than 2 times and 3 times than those of in water vapor (1Cr11Ni2W2MoV: 1.74 ± 0.26 mg/cm^2; Ti_2AlC coatings: 0.19 ± 0.04 mg/cm^2). Therefore, it could be proposed that NaCl seriously accelerated the corrosion process of 1Cr11Ni2W2MoV substrates and Ti_2AlC coatings at 600 °C. However, the mass gain of 1Cr11Ni2W2MoV substrates was largely reduced when the Ti_2AlC coatings were applied in both water vapor and solid NaCl deposits in water vapor conditions, demonstrating that the Ti_2AlC coatings significantly improved the corrosion resistance of bare 1Cr11Ni2W2MoV substrates.

3.3. Phase composition after 75 h corrosion at 600 °C

Fig. 4 shows the XRD patterns of 1Cr11Ni2W2MoV substrates and Ti_2AlC coatings after 75 h corrosion at 600 °C in both water vapor and NaCl deposit in water vapor. In addition to the Fe-Cr phase from the substrates, only X-ray diffraction peaks of Fe_2O_3 oxides were detected for 1Cr11Ni2W2MoV substrates in water vapor environment (Fig. 4a). The strong signal of the substrates and the low peak intensity of the Fe_2O_3 oxides represented a weak corrosion degree of the substrates. When exposed to environment of water vapor and solid NaCl, however, the substrates were corroded with the appearance of $FeCr_2O_4$ and Fe_2O_3 phases as well as residual NaCl, together with the disappeared diffraction peaks of substrates. This indicated that the thickness of corrosion products exceeded the XRD detection depth and the substrates underwent more serious corrosion in the presence of NaCl, which was consistent well with the corrosion kinetic results. As presented in Fig. 4b, in the case of Ti_2AlC coatings, only a small amount of corrosion products of rutile-TiO_2 (γ-TiO_2) were found after 75 h corrosion in water vapor environment. While, new corrosion products like $Na_4Ti_5O_{12}$, Na_2TiO_3 and $Na_2Ti_9O_{19}$, were detected in the presence of NaCl, suggesting that NaCl could further react with oxides to form metallic acid salts during corrosion process, which contributed to the faster corrosion rate of Ti_2AlC coatings. Moreover, the residual NaCl was found on the substrate surface after 75 h corrosion in solid NaCl deposit in water vapor disappeared for Ti_2AlC coatings at the same corrosion condition. Noted that Ti_2AlC MAX phase still remained the dominant phase even after 75 h corrosion, implying that Ti_2AlC coatings displayed superior corrosion resistance under synergistic effects of water vapor and solid NaCl at 600 °C.

3.4. Corrosion behavior of 1Cr11Ni2W2MoV substrates at 600 °C for 75 h

Fig. 5 compares the surface morphologies of the 1Cr11Ni2W2MoV

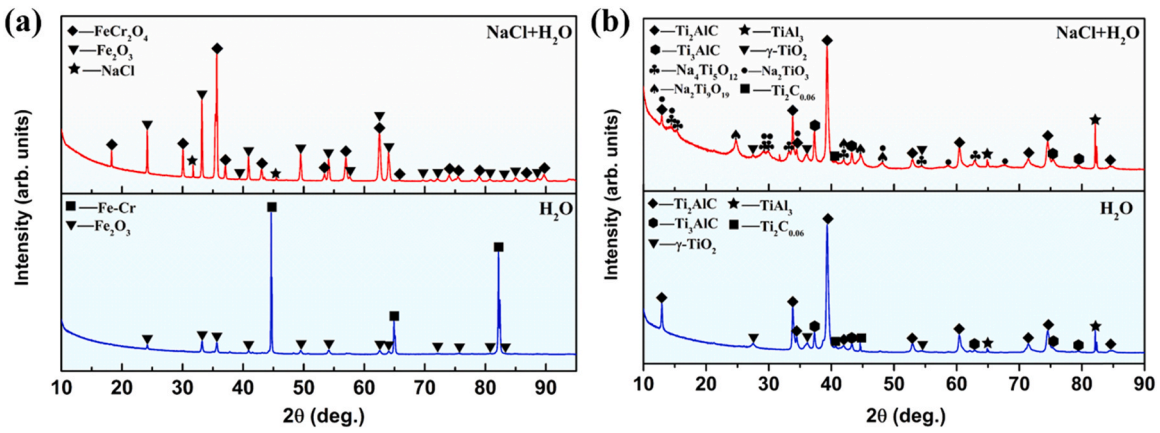

Fig. 4. XRD patterns of the 1Cr11Ni2W2MoV substrates (a) and Ti_2AlC coatings (b) after 75 h corrosion in H_2O and solid NaCl deposit in water vapor at 600 °C, respectively.

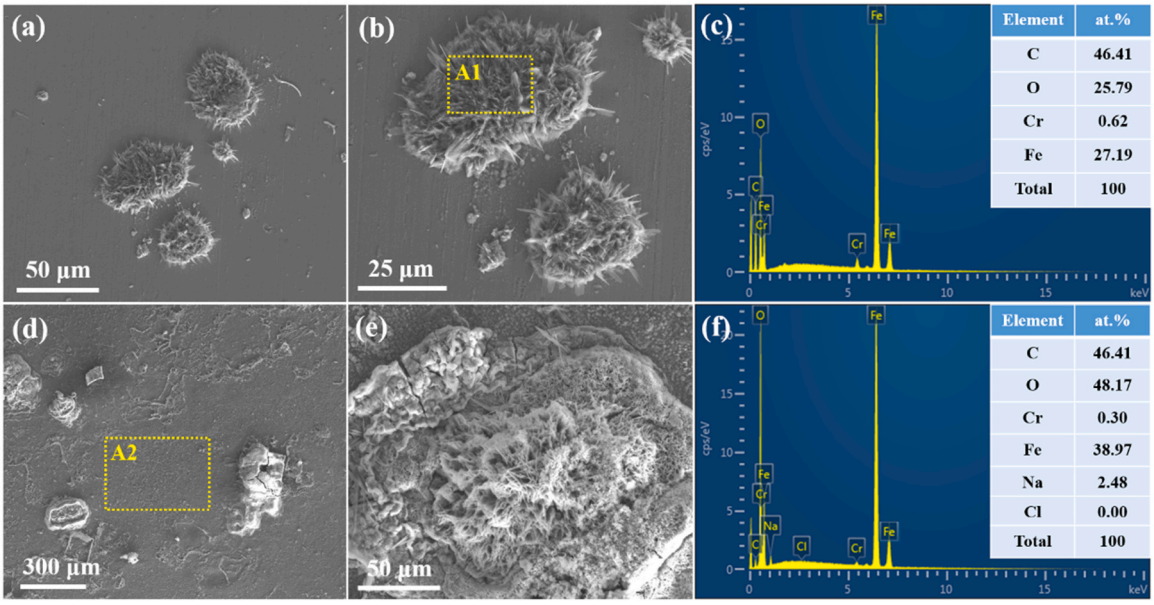

Fig. 5. Surface morphologies and EDS results of the 1Cr11Ni2W2MoV substrates after 75 h corrosion in different corrosion conditions: (a)–(c) water vapor; (d)–(f) solid NaCl deposit in water vapor. (a), (d) Low magnification; (b), (e) high magnification image; (c), (f) EDS profile from the rectangle area marked by yellow dotted line in (b) and (d).

substrates after 75 h corrosion at 600 °C in water vapor and solid NaCl deposit in water vapor, respectively, with corresponding EDS results. As shown in Fig. 5a and b, the needle-like oxides mainly appeared on partially localized surface areas for the substrates exposed in water vapor. The corresponding EDS results (Fig. 5c) acquired from the area "A1" in Fig. 5b indicated that these oxides were rich in Fe and poor in Cr, in agreement with the XRD results. Other areas without oxides aggregation remained smooth at low magnification images, probably because the thickness of the formed oxide layer was very thin. As reported in Ref. [25], the formed scale of Fe-Cr stainless steel in the initial oxidation stage was mainly composed of thin protective Cr-rich oxide layer. The water vapor would significantly accelerate the corrosion of stainless steel. The reason for the accelerated corrosion caused by water vapor was the vaporization of chromia scale from a protective Cr-rich oxide to a less protective $CrO_2(OH)_2$. As extending corrosion time, the Cr-rich scale would lose self-healing ability once the outer-diffusion rate of Cr was insufficient to maintain the needed Cr concentration in the scale. Then iron could diffuse easily outward to form non-protective needle--like Fe_2O_3 oxides.

Fig. 5d and e shows the surface morphologies of the substrates after corrosion in solid NaCl deposit in water vapor. It was found that oxide peeling and swelling occurred in the presence of NaCl (Fig. 5d), and there were obvious cracks and porosity within the swollen oxides, as seen from the enlarged image (Fig. 5e). In contrast to the corrosion results in water vapor, the EDS analysis from the area A2 (Fig. 5f) revealed that the surface oxides were also Fe-rich and Cr deficient after corrosion under synergistic effects of water vapor and solid NaCl, but containing more O element as a consequence of the accelerated corrosion of NaCl. Nevertheless, XRD results confirmed that the oxides were composed of Fe_2O_3 and $FeCr_2O_4$. Hence, it could be supposed that the corrosion scale possessed bilayer structure of a Fe_2O_3 upper layer and a $FeCr_2O_4$ down layer. Detailed discussion of this speculation is presented in the next section.

Fig. 6 displays the cross-sectional BSE image and corresponding EDS results of the 1Cr11Ni2W2MoV substrates after 75 h corrosion in water vapor at 600 °C. Fig. 6a given the cross-sectional morphologies of the corrosion region where was referred to the smooth area in Fig. 5a. It could be seen that the corrosion scale with ~ 6.5 μm thick was

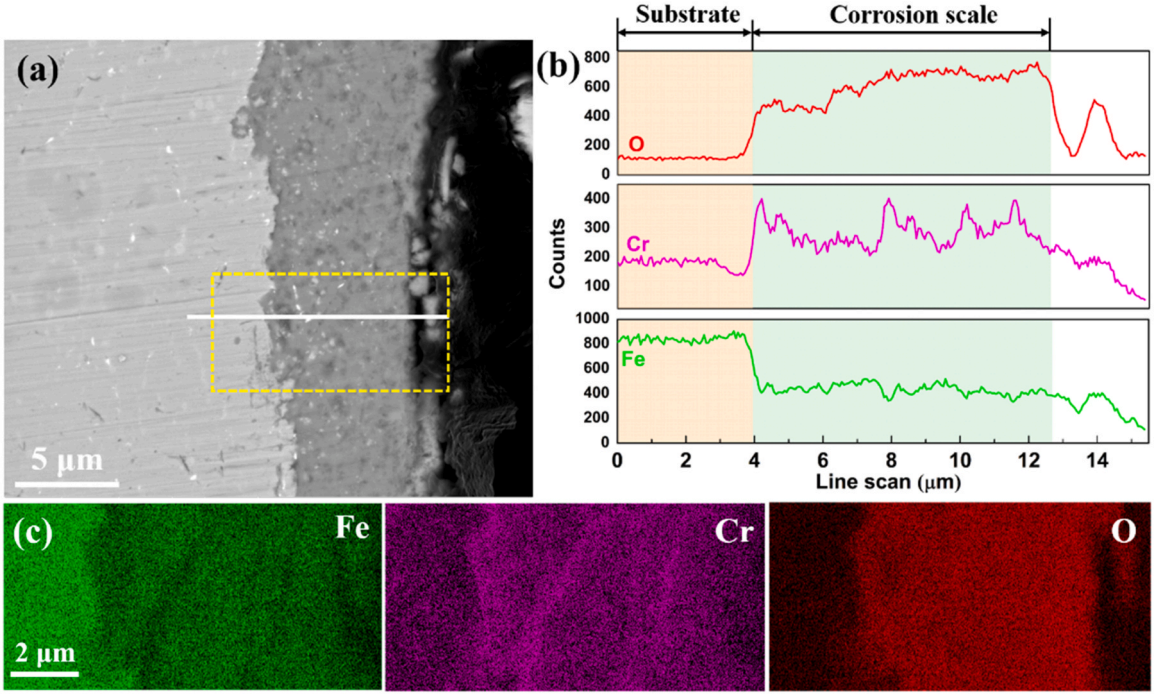

Fig. 6. (a) Cross-sectional SEM micrographs of the 1Cr11Ni2W2MoV substrates after 75 h corrosion in water vapor at 600 °C. (b) The corresponding line-scanning profiles of Fe, Cr and O elements along the white solid line in (a). (c) Fe (green), Cr (magenta) and O (red) elemental maps of the rectangle area marked by yellow dotted line in (a).

compacted and no blister or cracks were detected. EDS analysis (Fig. 6b and c) demonstrated the corrosion scale was enrich in Cr and poor in Fe, suggesting the possible formation of Cr_2O_3-rich oxides. However, apart from Fe_2O_3 phase, no Cr-related phases were observed in XRD results (Fig. 4a), which demonstrated that the formed Cr-rich oxides were likely amorphous or weak crystallization.

Fig. 7 shows the cross-sectional BSE image of the 1Cr11Ni2W2MoV substrates after 75 h corrosion at 600 °C in solid NaCl deposit with water vapor. It was obvious that the corrosion scale could be separated into two layers in which the outer layer contained some voids, as marked by the black arrows in Fig. 7a, while the inner layer appeared dense. The two layers were both even and continuous. The thickness of the whole

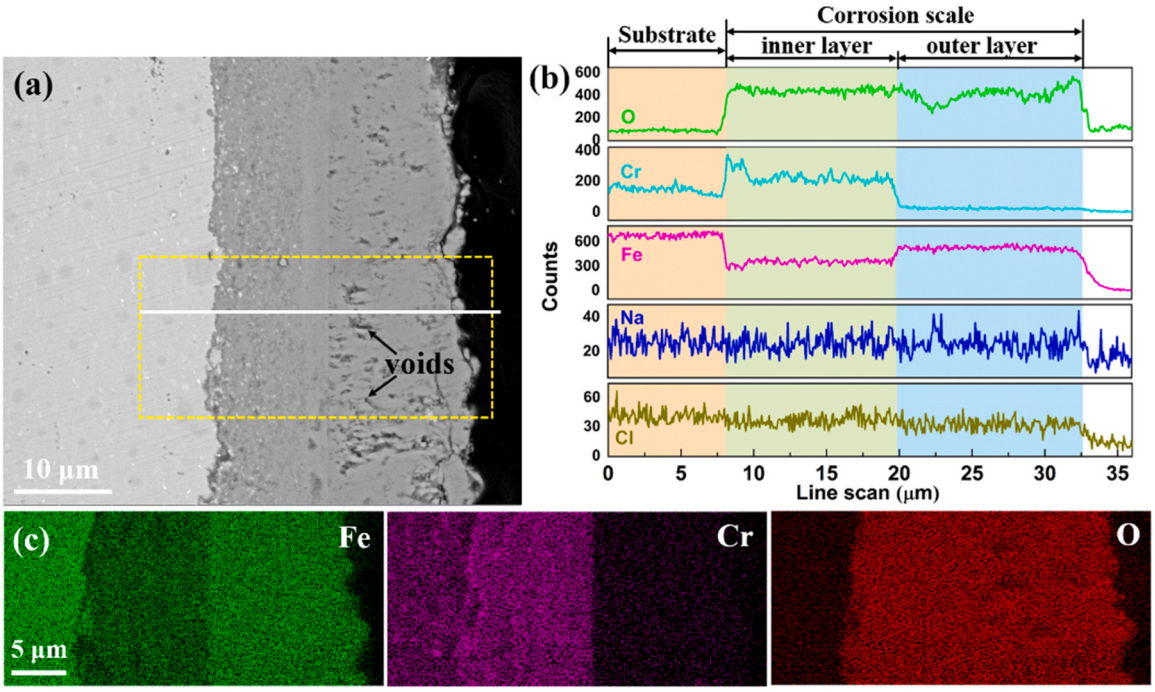

Fig. 7. (a) Cross-sectional SEM micrographs of the 1Cr11Ni2W2MoV substrates after 75 h corrosion in solid NaCl deposit in water vapor at 600 °C. (b) The corresponding line-scanning profiles of Na, Cl, Fe, Cr and O elements along the white solid line in (a). (c) Fe (green), Cr (magenta) and O (red) elemental maps of the rectangle area marked by yellow dotted line in (a).

corrosion scale was about 25 μm including an inner layer of ~ 11 μm and an outer layer of ~ 14 μm, which indicated that the inner layer was slightly less than the outer layer. The same results have been previously reported in Ref. [6]. The EDS line-scans along the white solid line and EDS maps, obtained from the yellow dotted area in Fig. 7a, were exhibited in Fig. 7b and c, respectively. The EDS results showed that the outer layer did not contain Cr and consisted exclusively of Fe and O, and the inner layer was enrich in Cr and poor in Fe. Based on the above XRD results, therefore, it was reasonable to conclude that the outer and inner layers were determined to be Fe_2O_3 and $FeCr_2O_4$ phases, respectively.

The above results indicated that 1Cr11Ni2W2MoV substrates suffered severe corrosion when exposed under synergistic effects of water vapor and solid NaCl. The severe corrosion has also been discussed in previously reported work [6], where comparative corrosion behaviors of Fe-20Cr under synergistic effects of water vapor and solid NaCl and NaCl solution spray, respectively, were conducted, and the underlying corrosion mechanism was elaborated as well. The adsorption and interdiffusion of a little transient Cl which destroyed the formation of protective Cr_2O_3 scale was assumed to play a key role in the acceleration corrosion of the Fe-20Cr. Thus, the corrosion mechanism of 1Cr11Ni2W2MoV was not in detail discussed in this study.

3.5. Corrosion behavior of Ti_2AlC coatings at 600 °C for 75 h

To evaluate the chemistry of the corrosion scale, Fig. 8 presents the primary XPS core-level spectra of the Ti_2AlC coatings corroded at 600 °C for 75 h in solid NaCl deposit with water vapor and in water vapor, respectively. The spectra of Al 2p (Fig. 8a) displayed two peaks at E_b ~ 71.7 eV and 74 eV in the water vapor, which were associated with the Ti_2AlC and Al_2O_3, respectively. While, one peak at E_b ~ 74 eV corresponding to Al_2O_3 was observed in solid NaCl deposit in water vapor. In the C 1s spectra, four peaks (E_b = 281.5, 283.7, 284.8 and 286.1 eV) emerged in water vapor due to the presence of Ti—C, Al—C, C—C and C—O bonds. However, Ti—C and Al—C bonds disappeared in solid NaCl deposit in water vapor, and meanwhile additional peak at 288 eV which ascribed to the C═O bond was visible. In both water vapor and solid NaCl deposit in water vapor, the O 1s indicated the same four peaks (E_b = 529.8, 530.9, 532.3 and 533.2 eV) associated with Al—O, O—Ti and O—H bonds as well as adsorbed O, respectively. Moreover, the Ti 2p spectra were fitted into four peaks, including two main peaks at 458.2 eV and 463.72 eV, and two shoulder peaks at 458.9 eV and 464.4 eV, corresponding to Na—Ti—O and Ti—O bonds, respectively, under the synergistic effects of water vapor and solid NaCl. But in the water vapor environment, the two main peaks located at E_b ~ 458.5 and 464.1 eV were assigned to Ti—O bonds, and the two shoulder peaks located at E_b ~ 457.7 and 463.3 eV corresponding to Ti—C bonds.

Fig. 9 gives the surface morphologies and corresponding EDS of the Ti_2AlC coatings after 75 h corrosion at 600 °C in water vapor and in solid NaCl deposit in water vapor, respectively. Similar to the surface morphologies of pristine Ti_2AlC coatings, no visible oxides with specific morphologies on their surface were formed after corrosion in water vapor (Fig. 9a). The corroded coatings still retained a dense structure, as seen from the enlarged image of Fig. 9b, demonstrating that the corrosion was mild in water vapor. Fig. 9c presents a typical EDS spectrum of the entire area of Fig. 9b. The corroded coating surface contained a certain amount of O (19.75 at%) and more C (53.82 at%), probably resulting from the oxides and the absorbed impurity, respectively. In contrast to the corrosion in water vapor, the corroded coatings in solid NaCl deposit in water vapor were consisted of compact oxides with

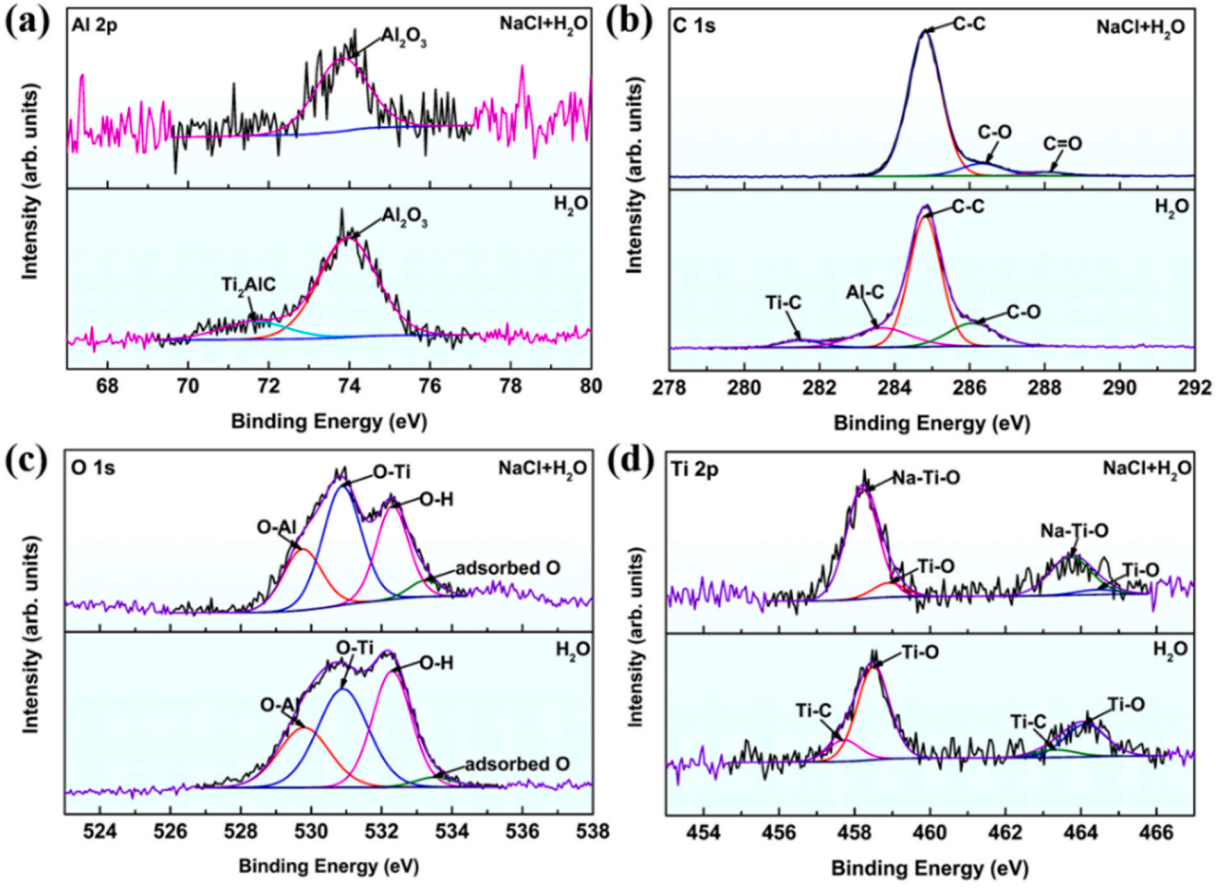

Fig. 8. (a) Al 2p, (b) C 1s, (c) O 1s, and (d) Ti 2p XPS core-level spectra of Ti_2AlC coatings after 75 h corrosion in water vapor and solid NaCl deposit in water vapor at 600 °C.

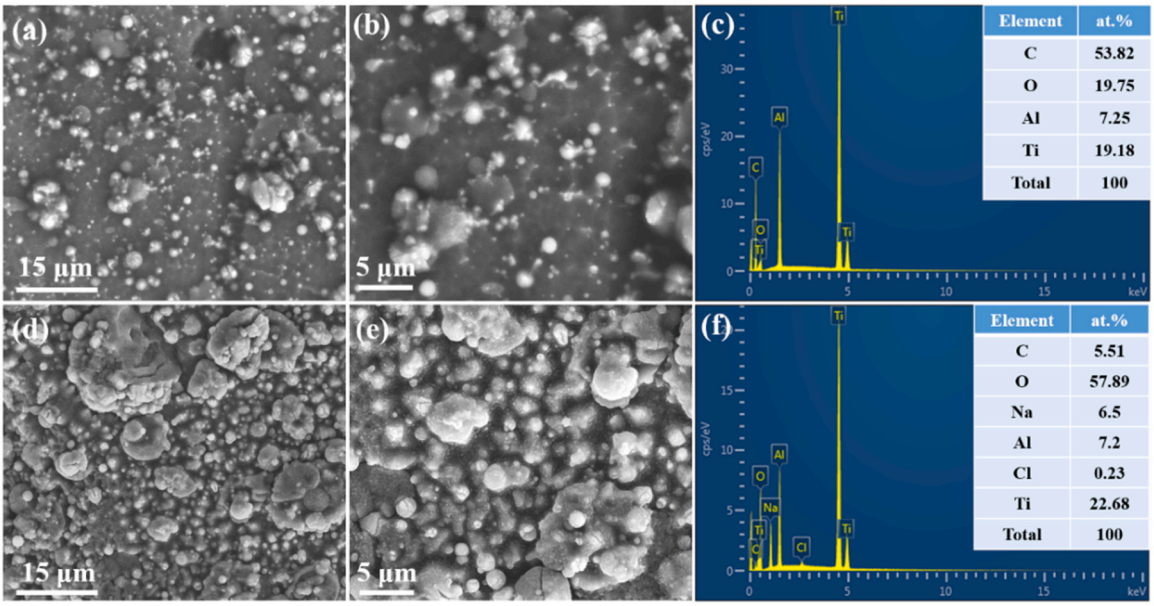

Fig. 9. Surface morphologies and EDS results of the Ti_2AlC coatings after 75 h corrosion in different corrosion conditions: (a)–(c) water vapor; (d)–(f) solid NaCl deposit in water vapor. (a), (d) Low magnification; (b), (e) high magnification image; (c), (f) EDS profile from the entire area of (b) and (e).

cauliflower-like structure (Fig. 9d), and the oxides clearly existed on the coating surface. This was related to varied composition of the oxides. Noted that spallation of the corrosion scale and obvious holes were invisible on the coating surface, except a few cracks emerged within the coarse oxide grains (Fig. 9e). According to the EDS analyses (Fig. 9f), the presence of 57.89 at% O and 5.51 at% C indicated a striking accelerated corrosion effect of water vapor and solid NaCl at high temperature. Moreover, probably because the formation of volatile species, such as $AlCl_3$(g), HCl(g), Cl_2(g), during corrosion process, the content of Cl element (0.23 at%) was much less than that of Na (6.5 at%) in the corrosion scale. Further discussion and quantitative results would be given in the later section.

To confirm the thickness, structure and composition of the formed corrosion scale of Ti_2AlC coatings in water vapor, the STEM measurement was conducted, and the corresponding results were shown in Fig. 10. Cross-sectional Z-sensitive STEM images (Fig. 10a) revealed that the Ti_2AlC coatings behaved non-uniform corrosion in water vapor. The oxide bumps, corresponding to the Ti macro-particles of pristine Ti_2AlC coatings, were identified to be TiO_2 based on the EDS mapping (Fig. 10c). Beneath the oxide bumps, the coatings were seriously corroded, and a loose corrosion scale with obvious voids was formed, as displayed in Fig. 10b. EDS mapping results demonstrated the loose corrosion scale was mainly consisted of TiO_2 with high defect density, which thereafter deteriorated the corrosion protection of the underlying coatings. Moreover, the enrichment of Al and O was detected at the corrosion scale/coatings interface, in line with the high activity of Al in Ti_2AlC MAX phase, which promoted Al to diffuse faster from the coating to interface. As expected, a compact and well adhered Al_2O_3 corrosion layer with ~ 50 nm thickness appeared on the coating surface, but the oxide bumps interrupted its continuity (Fig. 10b). This dense Al_2O_3 corrosion layer around the oxide bumps could prevent the underlying coatings from corroding. As a result, the Ti macro-particles formed during the coating deposition played a vital role in the corrosion behavior of the coatings, which accelerated the corrosion rate of the coatings in water vapor, as reported in our previous work [22].

Fig. 11 displays the cross-sectional morphologies and the EDS analyses of the Ti_2AlC coatings after 75 h corrosion under the synergistic effects of water vapor and solid NaCl at 600 °C. A compact and continuous corrosion scale with 3 μm thick was formed on the coating surface based on the contrast difference in Fig. 11a. The corrosion scale behaved dense and even structure without any defects, such as cracks, voids, spalling, etc., were identified by SEM, which was comparable to

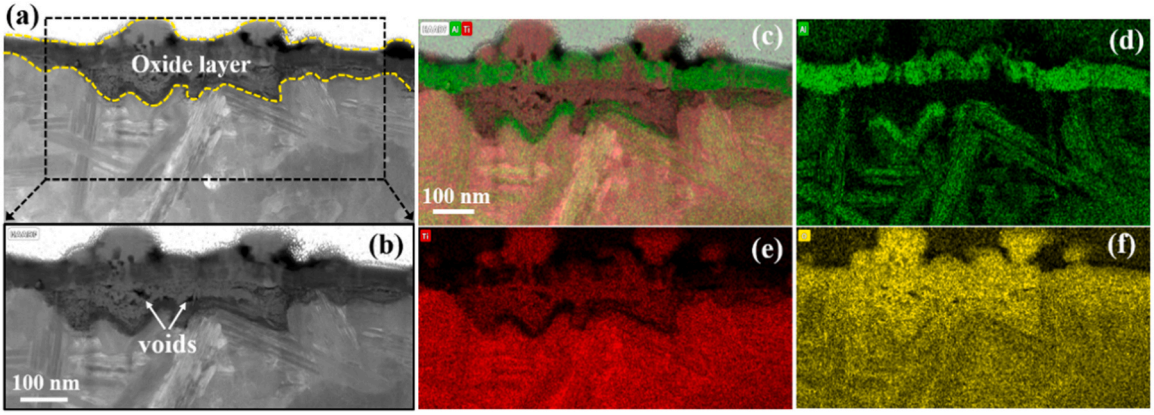

Fig. 10. (a) Low-magnification STEM image of the Ti_2AlC coatings after 75 h corrosion in water vapor at 600 °C. (b) High-magnification STEM image of the marked rectangle region as black dotted line in (a). (c) Ti-Al, (d) Al (green), (e) Ti (red) and (f) O (yellow) elemental maps of the region in (b).

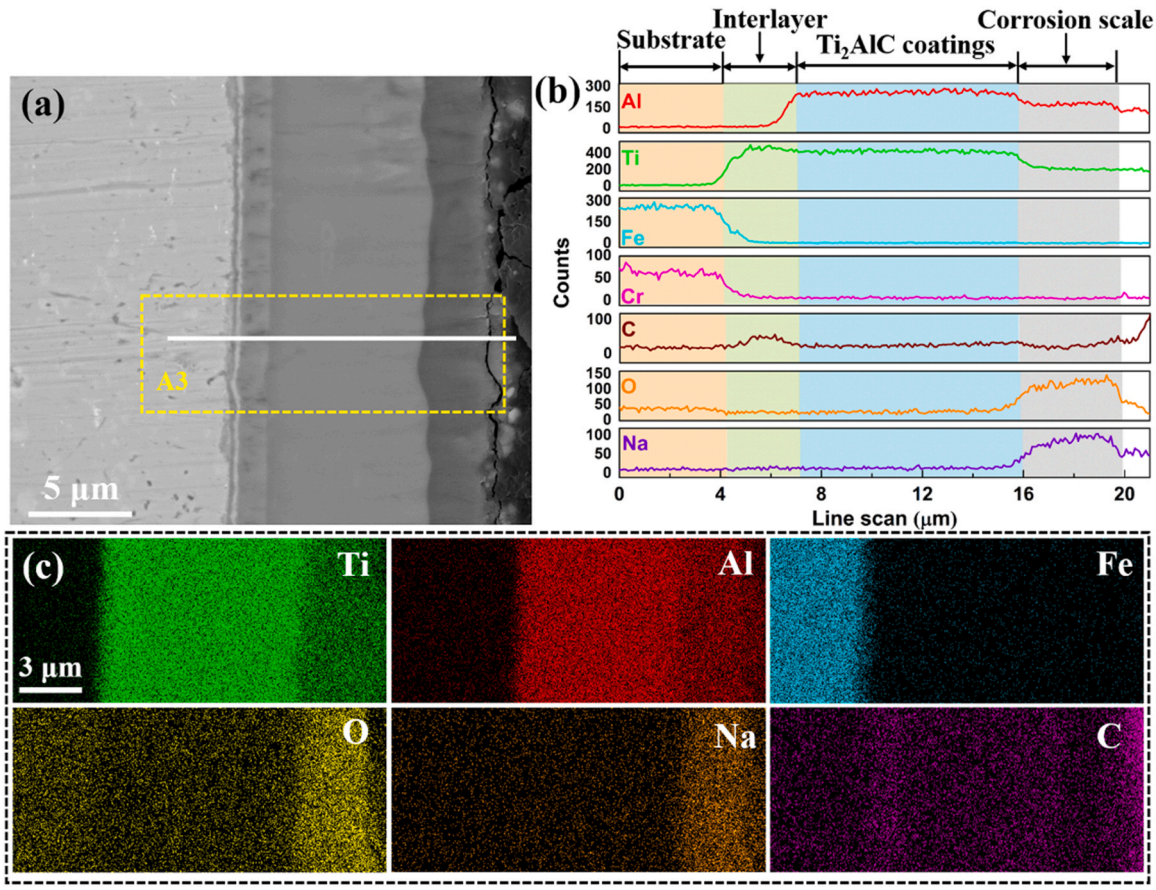

Fig. 11. (a) Cross-sectional SEM micrographs of the corroded Ti_2AlC coatings at 600 °C for 75 h in solid NaCl deposit in water vapor. (b) The corresponding line-scanning profiles of Al, Ti, Fe, Cr, C, O, Na elements along the white solid line in (a). (c) Ti (green), Al (red), Fe (sky-blue), O (yellow), Na (orange), and C (magenta) elemental maps of the marked rectangle region as yellow dotted line in (a).

the pristine Ti_2AlC coatings. The clear and relatively sharp interface between coating and corrosion scale revealed a strong adherent feature with each other even after mechanical polishing. The EDS line scanning profiles (Fig. 11b) along the white line in Fig. 11a and EDS mapping results (Fig. 11c), acquired from area "A3", indicated that the corrosion scale was mainly composed of Ti, Al, O and Na elements. However, no Al-containing corrosion products were detected by XRD patterns. Therefore, it was reasonable to assume that these Al-containing corrosion products are amorphous or weak crystalline. Furthermore, the concentration of O and Na dramatically decreased to a very low level at the coating/corrosion scale interface, suggesting that no inner corrosion occurred which benefited from the dense corrosion scale. Meanwhile, the presence of TiC interlayer could prevent elemental interdiffusion between the substrate and coating during corrosion process.

In an effort to systematically investigate the microstructure and composition of the corrosion scale, cross-sectional TEM characterizations were done, as displayed in Fig. 12. Fig. 12a showed the bright-field (BF) image of the corrosion scale, with corresponding inset SAED patterns. As expected, the corrosion scale consisted of dense structure with no discernable porosity and open boundaries. The SAED patterns, insets in Fig. 12a, were assigned to diffraction arcs of $Na_4Ti_5O_{12}$ phase with 012, 003, 110, 202, 023 and 204 components, but lack of Na_2TiO_3 and $Na_2Ti_9O_{19}$ phases confirmed by XRD results (Fig. 4). This could be explained by the limited amount of these formed phases. The average grain sizes of the $Na_4Ti_5O_{12}$ phase by the DF-TEM imaging (Fig. 12c) were determined to be 11 nm, and the measured grain sizes corrosion products span from 6 to 23 nm. In addition, the presence of $Na_4Ti_5O_{12}$ phase with (601) plane was also clearly evidenced by the HRTEM analyses (Fig. 12d). Fig. 13a was obtained using STEM-HAADF imaging mode depending on the atomic number (Z), where darker and brighter regions correspond to lower and higher Z, respectively. It was interesting to note that the corrosion scale displayed a nanocomposite structure, which included brighter regions surrounded by the darker regions. Combined with the XRD and cross-sectional EDS results, it could be speculated that the brighter regions corresponded to the sodium titanate ($Na_xTi_yO_z$), while the darker regions corresponded to the Al-containing oxide phases. This was demonstrated by the EDS mapping results (Fig. 13b–g). To get more insights into the formation of the corrosion scale, EDS analyses at different position of the scale denoted by small circles in Fig. 13a have been done, and the data was summarized in Table 1. EDS spectra 1 and 2 given the elementary composition inside the corrosion scale, where similar concentration was detected reflecting uniform corrosion, but Ti/Al atomic ratio deviated from that of in-corrosive region (EDS spectra 3) likely due to the formation of volatile chloride.

Fig. 14 further presents the high magnification HAADF-STEM and ADF-STEM image of the corrosion scale, respectively. As shown in Fig. 14a and b, the $Na_xTi_yO_z$ which exhibited bright region appeared, at this scale of a grain, to be nanocrystalline; while, the dark Al-enriched region forming the typical three dimensional (3D) network structure, enclosed several small crystallites of $Na_xTi_yO_z$. Fig. 14c shows the corresponding EDS maps of Ti and Al at the region from Fig. 14a. The EDS maps and EDS line profile (inserts in Fig. 14c) along the yellow arrow line in Fig. 14a confirmed the dark regions contained significant more Al than that in the bright region, which was agreement with the quantitative results of EDS spectra 4 and 5 (see Table 1). The HRTEM image of the dark Al-enriched region was shown in Fig. 14d. It was clear that Al-enriched region exhibited amorphous structure. Because Al_2O_3 is

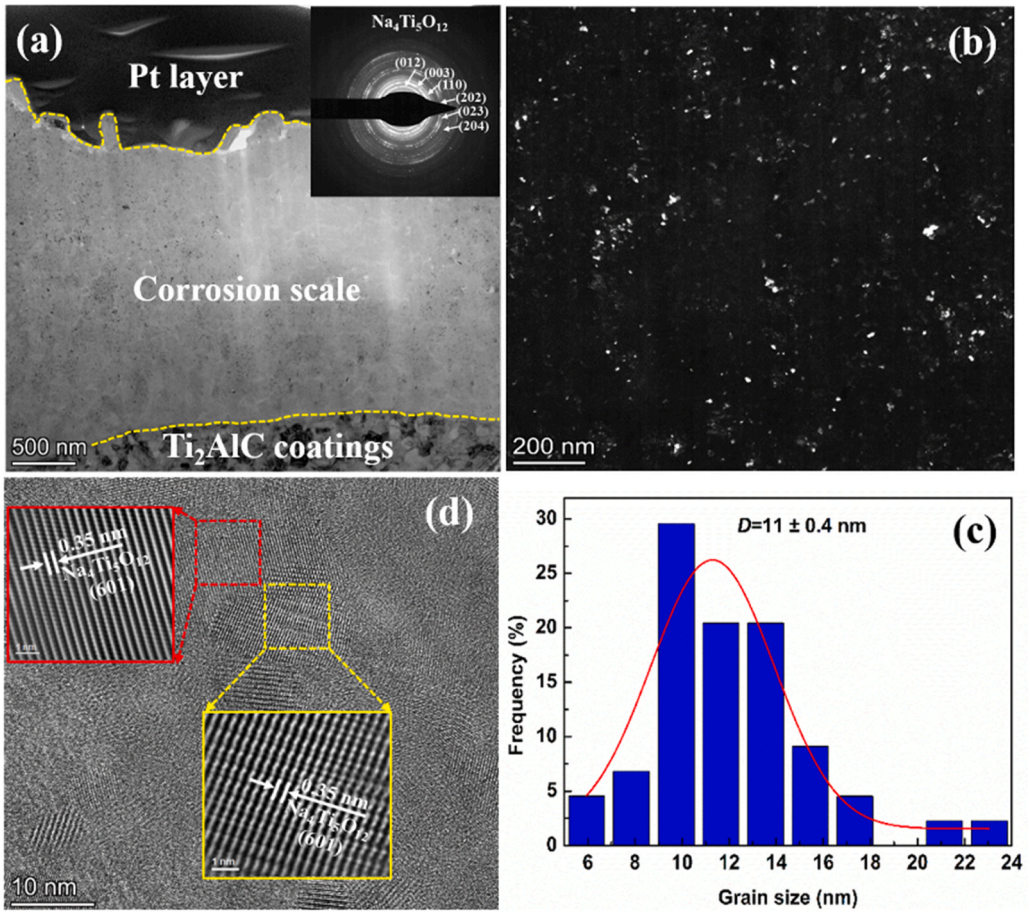

Fig. 12. TEM results of the corroded Ti_2AlC coatings at 600 °C for 75 h in solid NaCl deposit in water vapor. (a) TEM bright-field image of the corrosion scale with the corresponding SAED image. (b) TEM dark-field image, (c) the grain size distributions, and (d) HRTEM bright-field image of the corrosion scale.

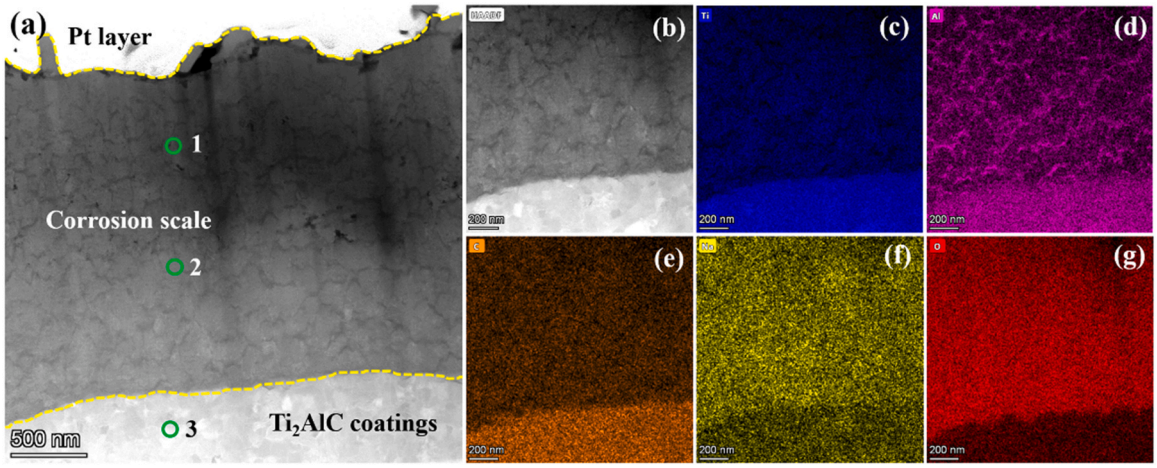

Fig. 13. (a) STEM image of the corrosion scale. (b) STEM image of the corrosion scale with higher magnification than that in (a) and the corresponding elemental maps of (c) Ti (blue), (d) Al (magenta), (e) C (orange), (f) Na (yellow), and (g) O (red).

preferentially formed based on the thermodynamical data, and Al_2O_3 is stable under H_2O-NaCl environment at 600 °C, and hence it is reasonable to infer that these Al-enriched amorphous tissues were Al_2O_3.

4. Discussion

4.1. Corrosion mechanism of Ti_2AlC coatings in water vapor

In water vapor, corrosion of Ti_2AlC coatings for 75 h at 600 °C caused a weight gain per unit area of 0.19 ± 0.04 mg/cm^2 (Fig. 3). The result was higher than the mass increase reported by Wang et al. [26] where the mass gain was less than 0.15 mg/cm^2 after 300 h oxidation at

Table 1
Chemical compositions (analyzed by EDS) of the points in Fig. 13a and 14a.

Point position	Elemental content (at%)				
	O	Na	Al	Cl	Ti
1	60.1	3.58	7.34	0.05	27.93
2	60	4.91	7.08	0.05	27.97
3	2.3	0.15	34.24	0.01	63.31
4	64.33	6.86	20.94	—	7.87
5	60	4.91	7.08	—	27.9

600 °C in air for Ti_2AlC coatings. Corrosion products here were mainly identified to be rutile TiO_2, consisted with previous observations [27]. Although the presence of Al_2O_3 was not detectable by XRD (Fig. 4), it was identified by XPS analysis (Fig. 8) at the top of the corrosion scale, which could be attributed to its relatively low content in contrast to that of TiO_2 phase. Moreover, some O-H bonds were visible under XPS results. According to Zeller et al. [28], the adsorption of water molecules at the surface of rutile TiO_2 were dissociated into OH^- and H^+ ions. Their dissolution within the TiO_2 layer might alter the nature of defects and thereby the transport mechanisms. Because of their smaller size compared to O^{2-}, OH^- is assumed to diffuse more rapidly [29], leading to faster corrosion kinetics.

In the Ti_2AlC MAX phase, it was deemed that the strong bonding between Ti and C together with weak bonding between Ti and Al remarkably decreased the activity of Ti, which consequently resulted in the preferential corrosion of Al [30]. Our results regarding corrosion scale structure and composition also revealed that Al preferentially diffused towards to the coating surface and formed Al_2O_3 layer during corrosion in water vapor, which could provide effective protection against corrosion of water vapor. However, the presence of Ti macro-particles interrupted its continuity, consequently resulting into the formation of loose corrosion region of TiO_2 with clear voids and micro-channels (Fig. 10).

Wang et al. [31] reported that the existence of hydrogen atom leaded to the accelerated corrosions as well. Since the release of hydrogen resulting from the dissociation of water vapor caused the formation of pores through the scale. These defects provided short-circuit diffusion channel for the inward diffusion of corrosive medium, such as water vapor and oxygen, and thus contributed to the improvement of the whole corrosion process. Although Ti_2AlC coatings underwent more severe corrosion in water vapor than that in air, corrosion scale especially at the compact Al_2O_3 region was as thin as 50 nm after 75 h corrosion at 600 °C in water vapor. Such result suggested that the corrosion rate was relatively slow and the Ti_2AlC coatings exhibited promising potential as protective coatings in water vapor.

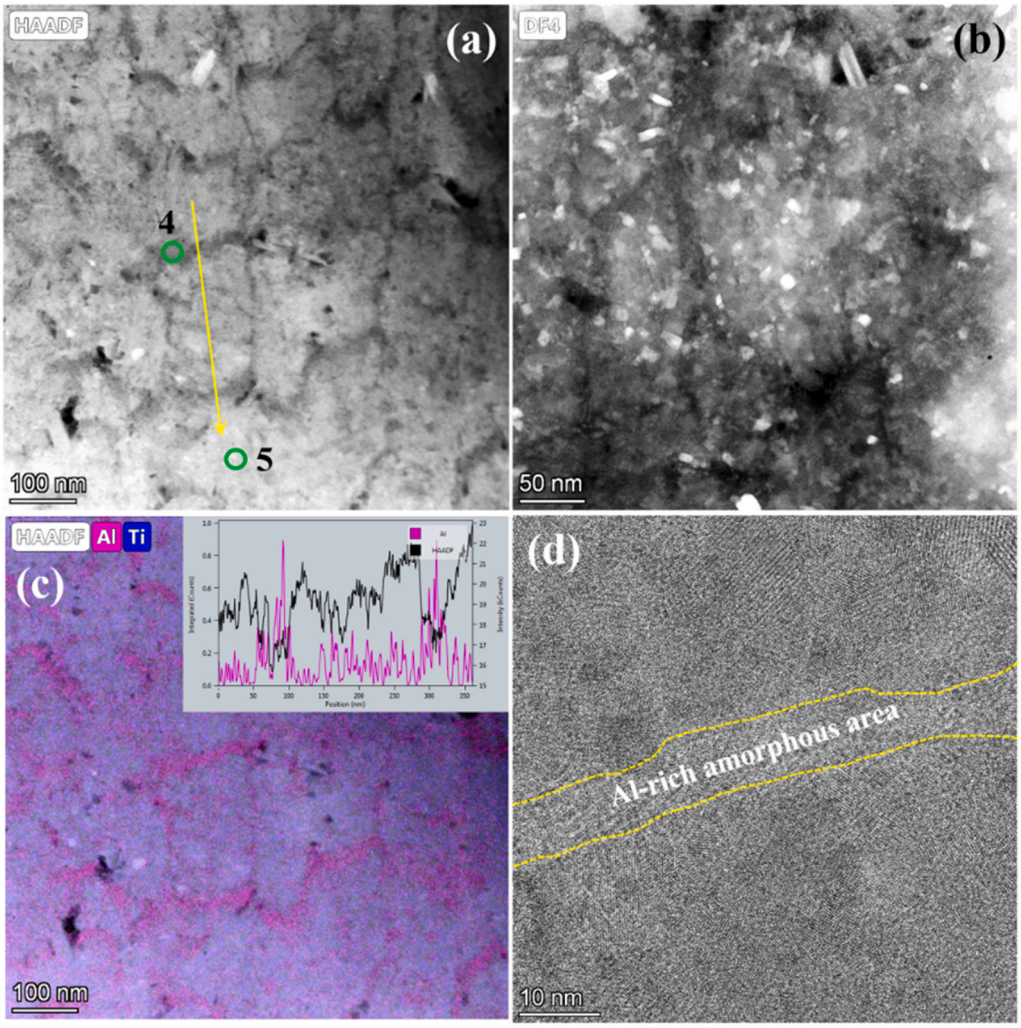

Fig. 14. TEM results of the corrosion scale of the Ti_2AlC coatings after 75 h corrosion at 600 °C in solid NaCl deposit in water vapor. (a) STEM-HAADF image. (b) STEM-ADF image. (c) Ti and Al elemental maps. (d) HRTEM image.

4.2. Synergistic corrosion mechanism of Ti_2AlC coatings under NaCl deposit in water vapor

The existence of NaCl salts was proved to be extremely deleterious for the Ti_2AlC coatings in water vapor at 600 °C, in which the weight gain per unit area (0.69 ± 0.09 mg/cm^2) was 3.6 times higher than that for NaCl-free coatings. This harmful influence of NaCl deposit on the corrosion resistance of Ti-based alloys and coatings has already been demonstrated in a number of studies [7,13,29,32–34]. The decreased corrosion resistance with the addition of NaCl deposit could be ascribed to an active corrosion mechanism. According to thermodynamic calculations in previous studies, this mechanism was activated due to the high vapor pressure of the $NaCl_{(s)} \leftrightarrow NaCl_{(g)}$ equilibrium at high temperature, which could even reach 1.8×10^{-6} bar at 600 °C [29]. As a result, based on the thermodynamics calculations listed in Table 2 and the mechanism proposed for other Ti-based materials, the corrosion of Ti_2AlC coatings in water vapor with NaCl deposit was dominated by the following series of reactions.

Firstly, during the corrosion experiment, the Ti_2AlC could be firstly oxidized generating TiO_2 and Al_2O_3, as shown in Eq. (1). However, the initially formed TiO_2 would be promptly destroyed in the early stage of its emergence because of the attack of chloride ion and water vapor. In fact, the main aggressive species ruining the oxide scale was $NaCl_{(g)}$, not $H_2O_{(g)}$, as reported by Ciszak et al. [35], at least for short exposure. The chemical reactions between NaCl, H_2O and TiO_2 were as follows Eqs. (2)–(4):

$$4Ti_2AlC(s) + 15O_2(g) \rightarrow 8TiO_2(s) + 2Al_2O_3(s) + 4CO_2 \quad (1)$$

$$5TiO_2(s) + 4NaCl(s) + 2H_2O(g) \rightarrow Na_4Ti_5O_{12}(s) + 4HCl(g) \quad (2)$$

$$TiO_2(s) + 2NaCl(g) + H_2O(g) \rightarrow Na_2TiO_3(s) + 2HCl(g) \quad (3)$$

$$9TiO_2(s) + 2NaCl(g) + H_2O(g) \rightarrow Na_2Ti_9O_{19}(s) + 2HCl(g) \quad (4)$$

Generally, the formed $Na_xTi_yO_z$ corrosion products including $Na_4Ti_5O_{12}$, Na_2TiO_3 and $Na_2Ti_9O_{19}$ exhibited porous structure, which could not protect the underlying coatings from corrosion [9]. Then, the generated $HCl_{(g)}$ migrated through the $Na_xTi_yO_z$ corrosion scale, and continued to react with the Ti_2AlC coatings. Both theoretical and experimental results demonstrated that Al in Ti_2AlC MAX phase owned a high diffusion rate and activity at high temperature, benefiting from its typical layered structure in which TiC-groups was separated by pure elemental Al layers [36]. Furthermore, the chlorine affinity of Ti was decreased greatly, because Ti atoms in Ti_2AlC were bound to carbon atoms by strong covalent and ionic bonding. Hence, Al was more preferably attacked by chlorine than Ti according to the Eq. (5):

$$2Ti_2AlC(s) + 6xHCl(g) \rightarrow 2Ti_2Al_{1-x}C(s) + 2xAlCl_3(g) + 3xH_2(g) \quad (5)$$

$$2Al(s) + 6HCl(g) \rightarrow 2AlCl_3(g) + 3H_2(g) \quad (6)$$

Since the weakly-bonded Al possessed high activity within the Ti_2AlC crystal structure, the thermodynamic calculation of reaction (5) was approximately determined by reaction (6). The formed $AlCl_{3\ (g)}$ would diffuse outward and reach region with high water vapor partial pressure to rapidly form Al_2O_3 and $HCl_{(g)}$, as suggested in Eq. (7). The accelerated corrosion in the presence of NaCl was referred to such an active oxidation process in this study. More importantly, the $AlCl_{3(g)}$ could migrate to the defects within the $Na_xTi_yO_z$ corrosion scale and react with H_2O to form Al_2O_3 oxides to fill these defects. As the formed $AlCl_3$ are in gaseous state, based on the heterogeneous nucleation principle, the reactions of chloride oxidation would preferentially occur on any defect (i.e. pore surface, material surface or crack surface) that would favor them energetically, similarly to what happened in chemical vapor deposition (CVD) processes [37].

$$2AlCl_3(s) + 3H_2O(g) \rightarrow Al_2O_3(s) + 6HCl(g) \quad (7)$$

As a consequence, the corrosion scale of Ti_2AlC coatings after 75 h corrosion in solid NaCl deposit in water vapor exhibited compact, uniform and nanocomposite structure, which effectively blocked the penetration of the atoms/particles. The formed fine crystalline grains of $Na_xTi_yO_z$ with size of 11 ± 0.4 nm easily result into creep deformation, in which the growth stress and thermal stress were easily released for the corrosion scale [38]. Thereby, the degradation of the corrosion scale was suppressed significantly, and the corrosion resistance of coatings was enhanced.

On the other hand, the defects filling by the Al_2O_3 amorphous phases in composite corrosion scale, as shown in Fig. 14, might be another factor to improve the resistance to salt corrosion of coatings. Because the Al_2O_3 was inert in an environment containing solid NaCl and water vapor, which could not react with solid NaCl and water vapor at 600 °C [32,39]. Although the Al_2O_3 corrosion products filled in the corrosion scale made no contribution to change the corrosion mechanism, it modified the structure of the corrosion scale and favored it more compact. Thus, achieving a dense corrosion scale modified by Al_2O_3, insensitive to Cl^- or H^+ ions, was advantageous to inhibit the rapid corrosion of Ti_2AlC MAX phase coatings at elevated temperature. Because it provided a barrier to inhibit the short-circuit inter-diffusion of aggressive ions such O_2, Cl^- and H_2O molecular into the coatings. Therefore, the persistent corrosion of the TiAl-based MAX phase coatings was prohibited [35]. The schematic process of corrosion was proposed in Fig. 15.

Table 2
The value of the standard Gibbs free-energy changes (ΔG°_{873K}) of the reactions (calculated with HSC9.0 software using the estimate databases).

	Chemical reaction	ΔG°_{873K} (kJ/mol)
(1)	$4Ti_2AlC(s) + 15O_2(g) \rightarrow 8TiO_2(s) + 2Al_2O_3(s) + 4CO_2(g)$	− 11,662.1
(2)	$5TiO_2(s) + 4NaCl(g) + 2H_2O(g) \rightarrow Na_4Ti_5O_{12}(s) + 4HCl(g)$	− 200.23
(3)	$TiO_2(s) + 2NaCl(g) + H_2O(g) \rightarrow Na_2TiO_3(s) + 2HCl(g)$	− 112.11
(4)	$9TiO_2(s) + 2NaCl(g) + H_2O(g) \rightarrow Na_2Ti_9O_{19}(s) + 2HCl(g)$	− 362.54
(5)	$2Ti_2AlC(s) + 6xHCl(g) \rightarrow 2Ti_2Al_{1-x}C(s) + 2xAlCl_3(g) + 3xH_2(g)$	—
(6)	$2Al(s) + 6HCl(g) \rightarrow 2AlCl_3(g) + 3H_2(g)$	− 482
(7)	$2AlCl_3(g) + 3H_2O(g) \rightarrow Al_2O_3(s) + 6HCl(g)$	− 320.932

5. Conclusion

Compared with weight gain per unit area in water vapor for 75 h, both the enhanced corrosion resistance was noticed for 1Cr11Ni2Mo2WV substrates and Ti_2AlC coatings by a factor of 2.5 and 3.6, respectively, due to the synergistic effect of NaCl deposit and water vapor at 600 °C. Noted that the mass gain per unit area of 1Cr11Ni2W2MoV substrates (4.3 ± 0.19 mg/cm^2) was largely reduced by applying Ti_2AlC coatings (0.69 ± 0.09 mg/cm^2). The corrosion scale on the 1Cr11Ni2Mo2WV in water vapor exhibited a Cr_2O_3-rich dense structure with the thickness of ~ 6.5 μm, but it consisted of two layered structure including an outer Fe_2O_3 layer with some obvious voids and an $FeCr_2O_4$ inner layer in the NaCl solution spray environment. For the Ti_2AlC coatings after 75 h corrosion in solid NaCl deposit in water vapor, the corrosion scale was bonded well with the uncorroded coatings and exhibited compact, uniform and nanocomposite structure. Because the defects within the $Na_xTi_yO_z$ corrosion scale during corrosion progress could be effectively self-healed by the Al_2O_3 amorphous phases, which were inert in water vapor and NaCl environment. Hence, the corrosion resistant properties of Ti_2AlC MAX phase coatings was further enhanced. The results not only provide the basic understanding on corrosion behavior of Ti_2AlC MAX phase coatings in various environments, but also bring forward the alternative promising applications for MAX phase coatings used in harsh steam corrosive conditions such as nuclear stack systems and aircraft engines.

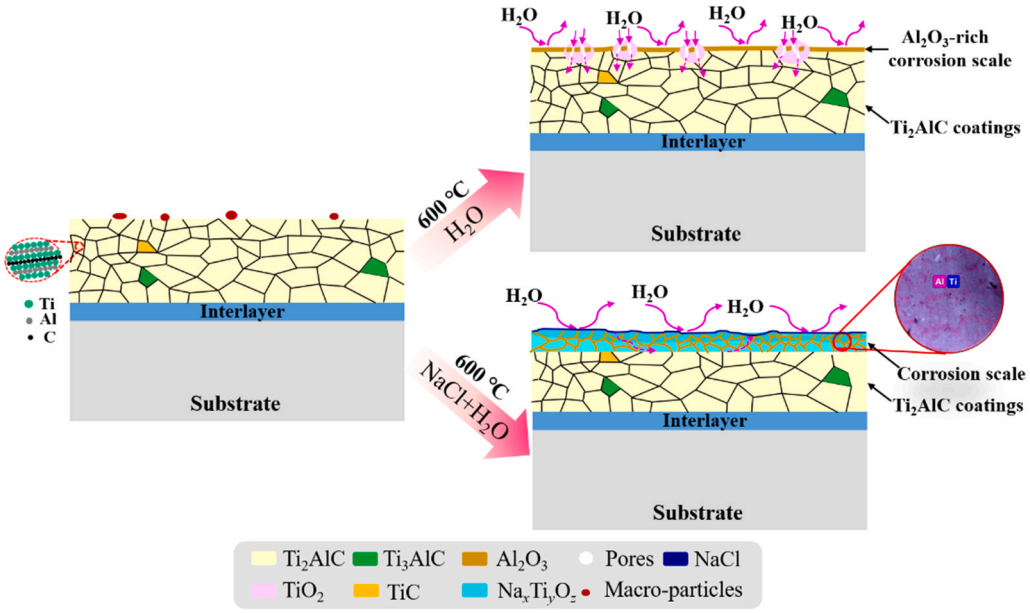

Fig. 15. Schematic diagram of the corrosion mechanism for the Ti_2AlC coatings under water vapor and solid NaCl deposits in water vapor at 600 ℃ for 75 h.

CRediT authorship contribution statement

Zhenyu Wang: Conceptualization, Methodology, Investigation, Data curation, Writing – original draft. **Guanshui Ma**: Validation, Writing – review & editing. **Zhongchang Li**: Resources, Visualization, Data curation. **Haitao Ruan**: Formal analysis, Investigation. **Jianghuai Yuan**: Validation, Investigation. **Li Wang:** Methodology, Investigation. **Peiling Ke**: Project administration, Writing – review & editing, Supervision. **Aiying Wang**: Writing – review & editing, Supervision.

Declaration of Competing Interest

The authors declare that they have no known competing financial interests or personal relationships that could have appeared to influence the work reported in this paper.

Data Availability

The data that support the findings of this study are available from the corresponding author upon reasonable request.

Acknowledgement

This research was supported by the National Science and Technology Major Project (2017-VII-0012-0108), National Natural Science Foundation of China (52025014, 52171090, 51901238), and Natural Science Foundation of Ningbo (202003N4025).

References

[1] T.J. Carter, Common failures in gas turbine blades, Eng. Fail. Anal. 12 (2005) 237–247.
[2] L. Fan, L. Liu, M. Cao, Z. Yu, Y. Li, M. Chen, F. Wang, Corrosion behavior of Ti60 alloy under a solid NaCl deposit in wet oxygen flow at 600 °C, Sci. Rep. 6 (2016) 29019.
[3] Y. Tang, X. Shen, Z. Liu, Y. Li, Effects of the different solid deposits on the corrosion behavior of pure Fe in water vapor at 500 °C, Scanning 2020 (2020), 6280725.
[4] L. Fan, L. Liu, Z. Yu, M. Cao, Y. Li, F. Wang, Corrosion behavior of Ti60 alloy under a solid NaCl deposit in wet oxygen flow at 600 °C, Sci. Rep. 6 (2016) 29019.
[5] L. Fan, L. Liu, Y. Cui, M. Cao, Z. Yu, E.E. Oguzie, Y. Li, F. Wang, Effect of streaming water vapor on the corrosion behavior of Ti60 alloy under a solid NaCl deposit in water vapor at 600 °C, Corros. Sci. 160 (2019), 108177.
[6] M. Cao, L. Liu, Z. Yu, L. Fan, L. Ying, F. Wang, Studies on the corrosion behavior of Fe-20Cr alloy in NaCl solution spray at 600 °C, Corros. Sci. 133 (2018) 165–177.
[7] L. Fan, L. Liu, Y. Lv, H. Wang, A. Fu, J. Yuan, Y. Li, F. Wang, C. Yin, Effects of pre-oxidation on the corrosion behavior of pure Ti under coexistence of solid NaCl deposit and humid oxygen at 600 °C: the diffusion of chlorine, Sci. Rep. 10 (2020) 16291.
[8] D. Zheng, S. Zhu, F. Wang, The influence of TiAlN and enamel coatings on the corrosion behavior of Ti6Al4V alloy in the presence of solid NaCl deposit and water vapor at 450 °C, Surf. Coat. Technol. 201 (2007) 5859–5864.
[9] R. Li, S. Wang, D. Zhou, J. Pu, M. Yu, W. Guo, A new insight into the NaCl-induced hot corrosion mechanism of TiN coatings at 500 °C, Corros. Sci. 174 (2020), 108794.
[10] C. Feng, M. Li, L. Xin, S. Zhu, F. Wang, Mechanical properties and oxidation behavior of a graded (Ti,Al)N coating deposited by arc-ion plating, Oxid. Met. 65 (2006) 307–327.
[11] Y. Li, L. Qu, F. Wang, The electrochemical corrosion behavior of TiN and (Ti,Al)N coatings in acid and salt solution, Corros. Sci. 45 (2003) 1367–1381.
[12] M. Zhang, L. Xin, X. Ding, S. Zhu, F. Wang, Effects Ti/TiAlN composite multilayer coatings on corrosion resistance of titanium alloy in solid NaCl-H_2O-O_2 at 600 °C, J. Alloy. Compd. 734 (2018) 307–317.
[13] M. Zhang, Y. Niu, L. Xin, J. Su, Y. Li, T. Wu, H. Zhao, Y. Zhang, W. Xie, S. Zhu, F. Wang, Studies on corrosion resistance of thick Ti/TiN multilayer coatings under solid NaCl–H_2O–O_2 at 450 °C, Ceram. Int. 46 (2020) 19274–19284.
[14] Z. Wang, J. Liu, L. Wang, X. Li, P. Ke, A. Wang, Dense and high-stability Ti_2AlN MAX phase coatings prepared by the combined cathodic arc/sputter technique, Appl. Surf. Sci. 396 (2017) 1435–1442.
[15] M. Haftani, M. Saeedi Heydari, H.R. Baharvandi, N. Ehsani, Studying the oxidation of Ti_2AlC MAX phase in atmosphere: a review, Int. J. Refract. Met. Hard Mater. 61 (2016) 51–60.
[16] Y.C. Zhou, X.H. Wang, Deformation of polycrystalline Ti_2AlC under compression, Mater. Res. Innov. 5 (2001) 87–93.
[17] V.D. Jovic, B.M. Jovic, S. Gupta, T. El-Raghy, M.W. Barsoum, Corrosion behavior of select MAX phases in NaOH, HCl and H_2SO_4, Corros. Sci. 48 (2006) 4274–4282.
[18] H.J. Yang, Y.T. Pei, J.C. Rao, J.T.M. De Hosson, Self-healing performance of Ti_2AlC ceramic, J. Mater. Chem. 22 (2012) 8304.
[19] Z. Wang, J. Sun, B. Xu, Y. Liu, P. Ke, A. Wang, Reducing the self-healing temperature of Ti_2AlC MAX phase coating by substituting Al with Sn, J. Eur. Ceram. Soc. 40 (2020) 197–201.
[20] Z. Wang, W. Li, Y. Liu, J. Shuai, P. Ke, A. Wang, Diffusion-controlled intercalation approach to synthesize the Ti_2AlC MAX phase coatings at low temperature of 550 °C, Appl. Surf. Sci. 502 (2020), 144130.
[21] Z. Wang, G. Ma, L. Liu, L. Wang, P. Ke, Q. Xue, A. Wang, Effect of homogenization-pressure-assisted enzymatic hydrolysis on the structural and physicochemical properties of lotus-seed starch nanoparticles, Int. J. Biol. Macromol. 167 (2021) 1579–1586.
[22] Z. Wang, X. Li, W. Li, P. Ke, A. Wang, Comparative study on oxidation behavior of Ti_2AlN coatings in air and pure steam, Ceram. Int. 45 (2019) 9260–9270.
[23] Z. Mahmoudi, S.H. Tabaian, H.R. Rezaie, F. Mahboubi, M.J. Ghazali, Synthesis of Ti_2AlC & Ti_3AlC_2 MAX phases by Arc-PVD using Ti–Al target in C_2H_2/Ar gas mixture and subsequent annealing, Ceram. Int. 46 (2020) 4968–4975.
[24] Y. Li, G. Zhao, Y. Qian, J. Xu, M. Li, Deposition and characterization of phase-pure Ti_2AlC and Ti $_3AlC_2$ coatings by DC magnetron sputtering with cost-effective targets, Vacuum 153 (2018) 62–69.

[25] Z.J. Feng, P.L. Ke, Q. Huang, A.Y. Wang, The scaling behavior andmechanismof Ti_2AlCMAX phase coatings in air and pure water vapor, Surf. Coat. Technol. 272 (2015) 380–386.
[26] Q.M. Wang, W. Garkas, A.F. Renteria, C. Leyens, H.W. Lee, K.H. Kim, Oxidation behaviour of Ti–Al–C films composed mainly of a Ti_2AlC phase, Corros. Sci. 53 (2011) 2948–2955.
[27] W. Li, Z. Wang, J. Shuai, B. Xu, A. Wang, P. Ke, A high oxidation resistance Ti_2AlC coating on Zirlo substrates for loss-of-coolant accident conditions, Ceram. Int. 45 (2019) 13912–13922.
[28] A. Zeller, F. Dettenwanger, M. Schütze, Influence of water vapour on the oxidation behaviour of titanium aluminides, Intermetallics 10 (2002) 59–72.
[29] C. Ciszak, I. Popa, J.-M. Brossard, D. Monceau, S. Chevalier, NaCl induced corrosion of Ti-6Al-4V alloy at high temperature, Corros. Sci. 110 (2016) 91–104.
[30] Z. Zhang, Y. Qian, J. Xu, J. Zuo, M. Li, Effect of annealing on microstructure evolution and corrosion resistance of an amorphous Cr-Al-C coating, Corros. Sci. 178 (2021), 109062.
[31] Z.-Y. Chen, L.-J. Wang, F.-S. Li, K.-C. Chou, Oxidation mechanism of Fe–16Cr alloy as SOFC interconnect in dry/wet air, J. Alloy. Compd. 574 (2013) 437–442.
[32] Y.H. Shu, F.H. Wang, W.T. Wu, Corrosion behavior of Ti60 alloy coated with a solid NaCl deposit in O_2 plus water vapor at 500–700 °C, Oxid. Met. 52 (1999) 463–473.
[33] Y. Liao, B. Zhang, M. Chen, M. Feng, J. Wang, S. Zhu, F. Wang, Self-healing metal-enamel composite coating and its protection for TiAl alloy against oxidation under thermal shock in NaCl solution, Corros. Sci. 167 (2020), 108526.
[34] Y. Xiong, S. Zhu, F. Wang, Synergistic corrosion behavior of coated Ti60 alloys with NaCl deposit in moist air at elevated temperature, Corros. Sci. 50 (2008) 15–22.
[35] C. Ciszak, I. Abdallah, I. Popa, J.-M. Brossard, A. Vande Put, D. Monceau, S. Chevalier, Degradation mechanism of Ti-6Al-2Sn-4Zr-2Mo-Si alloy exposed to solid NaCl deposit at high temperature, Corros. Sci. 172 (2020), 108611.
[36] Z.J. Lin, M.J. Zhuo, Y.C. Zhou, M.S. Li, J.Y. Wang, Microstructural characterization of layered ternary Ti_2AlC, Acta Mater. 54 (2006) 1009–1015.
[37] C. Christoglou, N. Voudouris, G.N. Angelopoulos, M. Pant, W. Dahl, Deposition of aluminium on magnesium by a CVD process, Surf. Coat. Technol. 184 (2004) 149–155.
[38] L.M. Chang, J.H. Liu, R.J. Zhang, Corrosion behaviour of electrodeposited Ni/Al_2O_3 composite coating covered with a NaCl salt film at 800 °C, Mater. Corros. 62 (2011) 920–925.
[39] X. Luo, Z. Ning, L. Zhang, R. Lin, H. He, J. Yang, Y. Yang, J. Liao, N. Liu, Influence of Al_2O_3 overlay on corrosion resistance of plasma sprayed yttria-stabilized zirconia coating in NaCl-KCl molten salt, Surf. Coat. Technol. 361 (2019) 432–437.